Photodissociation Dynamics of Cl₂O: Interpretation of Electronic Transitions†

Melanie Roth,‡ Christof Maul,* and Karl-Heinz Gericke

Institut für Physikalische und Theoretische Chemie, Technische Universität Braunschweig,
Hans-Sommer-Strasse 10, 38106 Braunschweig, Germany

The photodissociation of Cl_2O has been investigated for adjacent regions in the first and the second absorption bands, respectively, at dissociation wavelengths of 5.3 and 6.0 eV. Chlorine and oxygen atoms were state-selectively detected by resonance-enhanced multiphoton ionization. Chlorine fragment kinetic energy and spatial distributions were determined from time-of-flight profile analysis. At 5.3 eV, kinetic energy distributions are broad and bimodal and differ significantly for the two spin−orbit states $Cl^*(^2P_{1/2})$ and $Cl(^2P_{3/2})$. The decay is characterized by a positive anisotropy parameter of 0.7 ± 0.2. Excitation proceeds via the transitions $10a_1 \leftarrow 7b_2$ and $10a_1 \leftarrow 9a_1$. The data are in agreement with generating $ClO(X) + Cl^*(^2P_{1/2})$ as primary fragments. At 6.0 eV, kinetic energy distributions are narrow and structureless and are similar for the two spin−orbit states $Cl^*(^2P_{1/2})$ and $Cl(^2P_{3/2})$. The decay is characterized by a small positive anisotropy parameter of 0.2 ± 0.2. The main dissociation channel is the three-body decay into $2Cl + O$. The decay mechanism is of an asynchronous concerted type. The data suggest the primary production of $ClO(A) + Cl(^2P_J)$. Excitation proceeds mainly via the transition $8b_2 \leftarrow 7b_2$. The results show the need for refined theoretical calculations.

I. Introduction

Photochemistry and photophysics of Cl_2O have recently received considerable attention for several reasons.[1−10] The photochemistry of chlorine oxides is of general interest due to their role in atmospheric chemistry, although Cl_2O does not directly take part in the ozone depletion process in the stratosphere. Discrepancies in the assignment of its excited electronic states[6,10−12] exist, as well as disagreement between experimental and theoretical data with respect to its dissociation dynamics,[6,13,14] both of which have not completely been resolved until now. A most interesting feature of Cl_2O dissociation is the clean production of very highly rotationally excited ClO radicals.[9] Last, Cl_2O is an ideal candidate to study three-body decay processes,[15,16] due to its absorption spectrum extending into the easily accessible ultraviolet region and its relatively low three-body decay threshold of 4.18 eV. In particular, that all fragments in a three-body decay are atomic greatly simplifies the analysis of the experimental data.
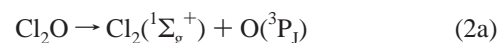
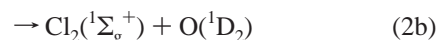For photon energies below 6.2 eV, several dissociation paths are energetically accessible:

$$Cl_2O \rightarrow Cl(^2P_J) + ClO(X^2\Pi_\Omega) \tag{1a}$$

$$\Delta H = 11\ 530\ cm^{-1} = 1.43\ eV \qquad \lambda_{thr} = 867\ nm$$

$$\rightarrow Cl(^2P_J) + ClO(A^2\Pi_\Omega) \tag{1b}$$

$$\Delta H = 43\ 180\ cm^{-1} = 5.35\ eV \qquad \lambda_{thr} = 231\ nm$$

$$Cl_2O \rightarrow Cl_2(^1\Sigma_g^+) + O(^3P_J) \tag{2a}$$

$$\Delta H = 13\ 710\ cm^{-1} = 1.70\ eV \qquad \lambda_{thr} = 729\ nm$$

$$\rightarrow Cl_2(^1\Sigma_g^+) + O(^1D_2) \tag{2b}$$

$$\Delta H = 29\ 580\ cm^{-1} = 3.67\ eV \qquad \lambda_{thr} = 338\ nm$$

$$\rightarrow Cl_2(^3\Pi_0^+) + O(^3P_J) \tag{2c}$$
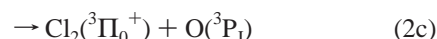
$$\Delta H = 31\ 540\ cm^{-1} = 3.91\ eV \qquad \lambda_{thr} = 317\ nm$$

$$Cl_2O \rightarrow 2\ Cl(^2P_J) + O(^3P_J) \tag{3}$$
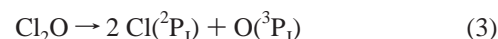
$$\Delta H = 33\ 710\ cm^{-1} = 4.18\ eV \qquad \lambda_{thr} = 296\ nm$$

Dissociation enthalpies, ΔH, are endoergicities for formation of the specified products at T = 0 K starting from Cl_2O molecules at $v = 0$ forming the J (respectively the Ω) components of the products with the lowest energy. The first pathway is the two-body decay, where a Cl atom and a ClO radical are generated. Excited $ClO(A^2\Pi_\Omega)$, if produced, is predissociative and characterized by lifetimes on the order of a few picoseconds or below, depending on fine-structure and vibrational states.[17] The second one is another two-body decay, which leads to a Cl_2 molecule and an atomic O fragment. Since Cl_2 elimination (reaction 2) will involve passage over an activation barrier, it is not expected to occur at the quoted λ_{thr} values. In both cases, the dissociation enthalpies depend on the product electronic states of the chlorine molecule and the oxygen atom or the ClO radical and the chlorine atom, respectively. The third pathway, the three-body decay,[15] produces two chlorine atoms and one oxygen atom.

Early photochemical work has been reviewed by Renard and Bolker.[18] The $Cl_2O(X^1A_1)$ ground-state electron configuration

Photodissociation Dynamics of Cl$_2$O

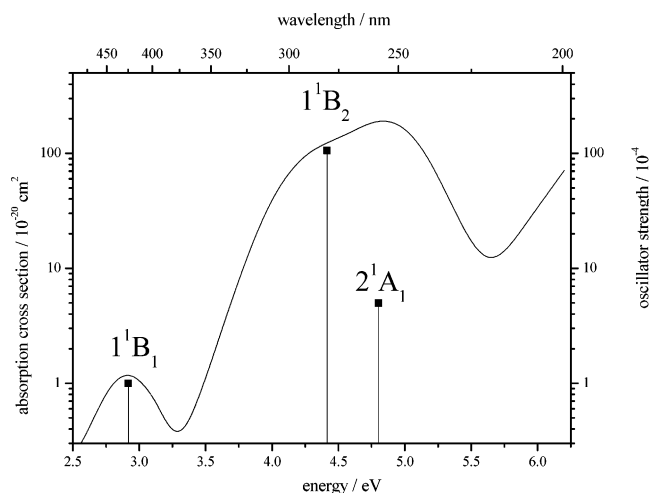*J. Phys. Chem. A, Vol. 108, No. 39, 2004* **7955**

Figure 1. Logarithmic representation of the Cl$_2$O absorption spectrum[28] and the three lowest electronic transitions suggested by Tomasello et al.[5] Transitions are mainly from nonbonding Cl(3p) orbitals to the lowest antibonding $\sigma^*(a_1)$ orbital. Squares represent the calculated oscillator strengths of the transitions at 2.92, 4.42, and 4.81 eV. Vertical axes have been scaled independently of each other.
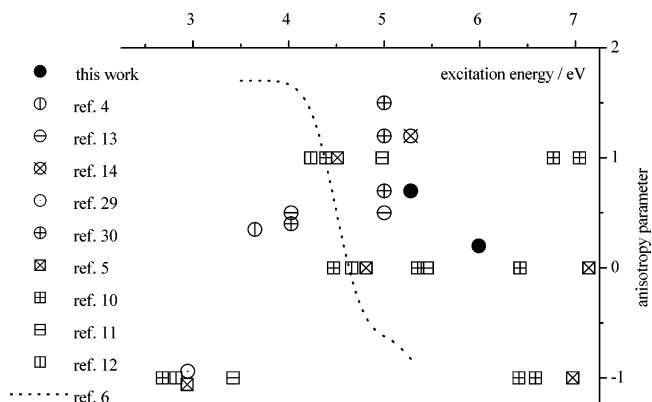

Figure 2. Experimentally observed Cl fragment anisotropy parameters and its limiting values as derived from theoretical calculations without considering simultaneous excitation of several states. Theoretical work is represented by open squares and the dotted line, respectively; experimental data are marked by circles. Filled circles are data obtained in this work. Experiments yield positive anisotropy parameters throughout the energy range between 3.5 and 6.5 eV. Theory predicts zero or negative limiting values between 4.5 and 6.5 eV.

is [core] $(6a_1)^2$ $(5b_2)^2$ $(7a_1)^2$ $(6b_2)^2$ $(8a_1)^2$ $(2b_1)^2$ $(2a_2)^2$ $(9a_1)^2$ $(7b_2)^2$ $(3b_1)^2$ $(10a_1)^0$ $(8b_2)^0$. The six highest occupied molecular orbitals are essentially contributed to by Cl(3p) and O(2p) electrons, which are in principle nonbonding, whereas the two lowest unoccupied orbitals can be identified as Cl–O antibonding σ^* orbitals. The energetic order of the occupied orbitals has unequivocally been determined by photoelectron spectroscopy.[1,2,19–21] Although photofragmentation is possible for wavelengths below 867 nm, Cl$_2$O absorption only starts with a very weak band centered at 510 nm, which is probably associated with a singlet–triplet excitation. Four more absorption features can be distinguished at 410, 285, 256, and 171 nm.[22–28] The absorption spectrum of Cl$_2$O below 500 nm is shown in Figure 1, together with the three lowest singlet–singlet transitions suggested by Tomasello et al.[5] Accordingly, the first strong absorption peak at 410 nm can be identified as $10a_1 \leftarrow 3b_1$ excitation into the 1^1B_1 state, whereas the broad feature with apparent maxima at 285 and 256 nm involves contributions from two transitions, the $10a_1 \leftarrow 7b_2$ excitation into the 1^1B_2 state being the dominant one, accompanied by the much weaker $10a_1 \leftarrow 9a_1$ transition into the 2^1A_1 state. The $10a_1 \leftarrow 2a_2$ transition, which is calculated to have a similar excitation energy, is dipole-forbidden and not assumed to contribute to the absorption spectrum. Most probably, the next main feature at higher energies in the absorption spectrum is predominantly caused by the three dipole-allowed transitions from the same $7b_2$, $9a_1$, and $2a_2$ orbitals into the second $8b_2$ Cl–O antibonding orbital.[5,11] The corresponding $8b_2 \leftarrow 3b_1$ transition is unlikely to play a significant role because it is dipole-forbidden. However, it has also been suggested that this second group of transitions should significantly contribute to the first absorption feature below 5.5 eV.[10] To resolve this issue by investigating the dissociation dynamics in the energy range between 5 and 6 eV has been one of the main objectives of the present work.

Experimentally, the photochemistry of Cl$_2$O has previously been investigated by several groups.[4,13,14,29,30] The dominating dissociation channel depends on the excitation energy and the excited state associated with the respective transition. Results concerning the fragment spatial distribution, based on the β anisotropy parameter, are summarized in Figure 2. Data generally refer to reactions 1 or 3, with excitation energies below

4.18 eV restricted to reaction 1a. The data displayed in Figure 2 clearly demonstrate the existing discrepancies concerning the ultraviolet dissociation of Cl$_2$O and the necessity to gather additional experimental information. Whereas the photodissociation and the corresponding states at low excitation energy below 4 eV (above 300 nm) are well characterized today, the situation is less clear for shorter wavelengths. Therefore, excitation energies of 5.3 and 6.0 eV (235 and 207 nm), which lie on different sides of a minimum in the absorption spectrum, were chosen so that dissociation should start on different potential energy surfaces of the molecule. The goal of the present work is to analyze the nature of the relevant excited states of Cl$_2$O on the basis of the state-specific spatial fragment distributions and to investigate the competition between two- and three-body decay on the basis of the fragment kinetic energy distributions by monitoring Cl fragments from Cl$_2$O photodissociation by the state-selective resonance-enhanced multiphoton ionization (REMPI) technique and analyzing the widths and the shapes of the corresponding time-of-flight (TOF) profiles.

At a dissociation energy of 2.9 eV (423 nm), Davis and Lee employed the photofragment translational spectroscopy technique and observed a negative anisotropy parameter, $\beta = -1$, for atomic chlorine fragments resulting from reaction 1a, thus confirming excitation of Cl$_2$O from the X^{1}A$_1$ ground state into a state of B$_1$ symmetry.[29] Around 3.6 eV (340 nm), ground-state ClO(X$^2\Pi_\Omega$) fragments also resulting from reaction 1a were state-selectively detected by Aures et al. with extremely high rotational angular momentum.[4] The ClO anisotropy parameter was found to be slightly positive, indicating a mild preference for fragment ejection parallel to the electric field vector of the dissociation laser light. The positive value of the anisotropy parameter is evidence of accessing a state of B$_2$ symmetry, as predicted by the majority of ab initio studies.[5,10,12] However, the experimental results of Aures et al. disagree with the association of the absorption around 350 nm (3.5 eV) with excitation into the ^{1}B$_1$ state as suggested by Nickolaisen et al.[11] Okumura and co-workers examined the dissociation at 308 (4.0 eV), 248 (5.0 eV), and 193 nm (6.4 eV) by photofragment translational spectroscopy (PTS).[13,30] With the exception of the three-body decay channel, which is not allowed energetically at 308 nm, all channels (1) through (3) are energetically accessible at all wavelengths. For all excitation wavelengths, two-body decay yielding ClO radicals was observed. Addition-

ally, at 248 and 193 nm three-body decay was observed, whereas two-body decay yielding molecular Cl_2 was only found to occur at 193 nm. The spatial fragment distribution was monitored for the ClO fragment for the longer wavelengths and for the O atom at 193 nm. In all cases, the anisotropy parameter, β, was found to be positive, indicating a preference for fragment ejection parallel to the electric field vector of the dissociation laser light. The positive value of the anisotropy parameter for the ClO products formed at 308 and 248 nm is again evidence of accessing a state of B_2 symmetry from the A_1 ground state, in agreement with the large oscillator strength found for the $1^1B_2 \leftarrow X^1A_1$ transitions in all available quantum mechanical calculations.[5,10–12] Last, Tanaka et al.[14] showed state-specific energy distributions for the $Cl(^2P_{3/2})$ ground state and the $Cl*(^2P_{1/2})$ excited spin–orbital state, markedly different from each other, by monitoring chlorine fragments in a photofragment ion-imaging experiment at an excitation energy of 5.3 eV (235 nm). From the Cl fragment kinetic energy distributions, they propose a competition between two- and three-body decay upon excitation of a single excited state. From the observed anisotropic behavior characterized by a large positive β parameter, this state was again identified to be of B_2 symmetry. Whereas the 5.3 eV experimental results are in reasonable agreement with the theoretical work of Nickolaisen et al.[11] and of Tomasello et al.,[5] unfortunately these findings contradict dynamical calculations by Toniolo et al.[10] in which quasi-classical trajectory calculations on the initially excited potential energy surface yielded a negative anisotropy parameter.

II. Experimental Section

Cl_2O gas was generated by the method of Cady,[31] where a gas mixture of N_2(900 mbar) and Cl_2(100 mbar) flows through a column filled with Hg(II)O and the reaction n HgO $+$ $2Cl_2$ $\rightarrow Cl_2O + HgCl_2 \cdot (n-1)$HgO takes place. The reaction product is purified by vacuum distillation at a temperature of ca. 200 K, maintained by a mixture of methanol and liquid nitrogen. This procedure leaves Cl_2, HOCl, and OClO as known impurities. After purification, the absorption spectrum of the sample was measured with a Lambda 9 Perkin-Elmer spectrometer. Fitting a superposition of the known absorption spectra of Cl_2O and the suspected impurities to the measured spectrum yielded that the sample consists of 51% Cl_2O, 33% Cl_2, 15% HOCl, and 1% OClO. In the wavelength region of interest (200–240 nm), only Cl_2O and HOCl have a nonvanishing absorption cross section, with the Cl_2O cross section being larger by a factor of 6. Therefore, the contribution to the signal caused by dissociation of HOCl cannot exceed 2.5% and can, therefore, be neglected in the data analysis procedure. It is evident, however, that for experiments carried out at longer dissociation wavelengths, additional effort has to be spent to remove interference from impurities.

The experimental setup is of the typical pump and probe type and has been described in detail elsewhere.[32,33] Cl_2O gas, as produced in the procedure described above, was mixed with argon in a ratio of approximately 1:10 to a total pressure of 10^5 Pa and was expanded into the time-of-flight (TOF) spectrometer region of a vacuum chamber in a supersonic jet produced by a pulsed nozzle (General Valve Series 9). The base pressure in the vacuum chamber without the jet was 0.1 Pa. At typical repetition rates of 10 Hz, the base pressure increased by 1 or 2 orders of magnitude, depending on the nozzle operating conditions. Typically, under these conditions, molecules are cooled to temperatures below 15 K.[34]

The supersonic molecular beam in the TOF spectrometer was crossed by the dissociation and the probe lasers, and the fragments were analyzed by the resonance-enhanced multiphoton ionization (REMPI) technique. Cl atoms were detected by (2+1) REMPI in the $^2P_{3/2}$ ground state and in the $^2P_{1/2}$ excited state. For the $^2P_{3/2}$ ground state, the ($4p^2\ ^2D_{3/2} \leftarrow {}^2P_{3/2}$) transition at 235.336 nm was employed; for the $^2P_{1/2}$ excited state, the ($4p^2\ ^2S_{1/2} \leftarrow {}^2P_{1/2}$) transition at 235.205 nm was used.[35,36] O atoms were detected by (2+1) REMPI in the $^3P_2$ state via the ($^3P_2 \leftarrow {}^3P_2$) transition at 225.57 nm.[37] The probe laser light was delivered by an excimer laser pumped dye laser (Lambda Physik LPX 100, LPD 3000, Coumarin 47) and was frequency doubled by a β barium borate (BBO) crystal. The probe pulse energy was kept in the range between 100 and 200 μJ and was focused into the ionization region of the TOF spectrometer by a lens of 80 mm focal length. For the 235 nm dissociation, the probe laser was also used as the dissociation laser (one-color experiment). For the 207 nm dissociation, light from a second, Nd:YAG laser pumped dye laser was used (Coherent Infinity, Lambda Physik Scanmate, Furan 2), which counter-propagated the probe laser beam (two-color experiment). The dissociation laser light was frequency doubled by a second BBO crystal. Typically, 200 μJ/pulse was focused into the TOF spectrometer by a lens of 90 mm focal length. A delay generator (Stanford Research DG 535) adjusted a delay of typically 10 ns between dissociation and probe pulses to ensure collision-free detection of the fragments. A $\lambda/2$ wave plate allowed for the rotation of the polarization of the dissociation laser in order to realize parallel and perpendicular detection geometries. Here, the angle, γ, of the electric field vector, $\vec{E}$, of the dissociating laser with respect to the TOF spectrometer axis, z, defines the terms parallel ($\gamma = 0°$) and perpendicular ($\gamma = 90°$).

The energy-sensitive home-built single-field TOF spectrometer has a total length, s, of 57 cm and consists of acceleration and drift regions, separated from each other by a grid, with a length ratio of 1:2. This arrangement ensures space-focusing conditions. The spectrometer axis, z, is oriented perpendicular to the plane defined by the molecular and laser beams. The acceleration field could be varied between 0 and 20 kV/m, resulting in minimum times of flight, t_0, of 5 μs for chlorine ions. Ions were monitored by a 4 cm active-diameter microchannel plate, and the transient, energy-broadened mass peak was recorded as the corresponding TOF profile $P_t(t)$ by a 350 MHz digital oscilloscope (LeCroy 9450), interfaced to a personal computer. The width and the shape of the transient TOF profiles $P_t(t)$ are measures of the initial kinetic energy and spatial distributions of the fragments obtained in the dissociation process. With respect to profile width, for our spectrometer geometry, the deviation, Δt, of the observed time of flight, t, from the center, t_0, of a TOF profile is proportional to the initial velocity component, v_z, of the observed fragment along the spectrometer axis, z:

$$\Delta t = 3t_0^2 v_z/(8s) \tag{4}$$

Thus, the distribution, $P_z(v_z)$, of the velocity component, v_z, onto the fragments is directly reflected in the experimental TOF profile: $P_z(v_z) \propto P_t(\Delta t)$. Since $P_z(v_z)$ depends on the chosen detection geometry, the initial spatial fragment distribution can be investigated by rotating the dissociation laser polarization.

The energy resolution of the spectrometer is typically 5%, depending on the acceleration voltage. All TOF profiles were monitored for different acceleration fields in order to exclude experimentally induced artifacts.

To increase the kinetic energy resolution of the experiment, TOF profiles obtained at moderate acceleration field strengths of 5 kV/m were analyzed. While increasing the energy resolu-
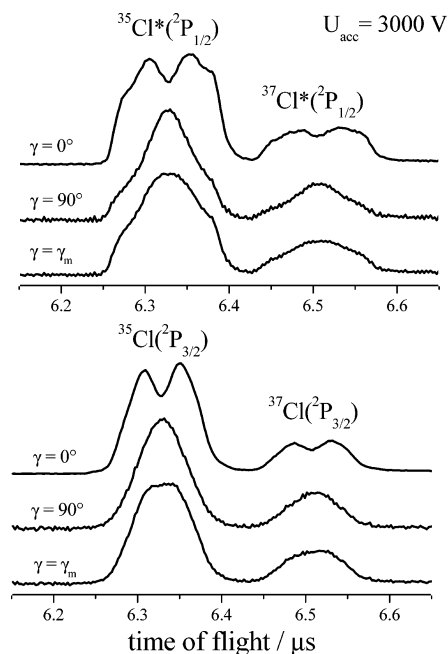
Figure 3. Cl atom TOF profiles for Cl₂O dissociation at 5.3 eV (235 nm). All profiles have been normalized with respect to their integrated areas. Profiles are shown for both Cl($^2P_{3/2}$) and Cl*($^2P_{1/2}$) spin−orbit states with perpendicular ($\gamma = 90°$) and parallel ($\gamma = 0°$) detection geometry at an acceleration voltage $U_{acc} = 3$ kV. Magic angle profiles ($\gamma = \gamma_m$) were computed from the weighted sum of the raw profiles. Profiles reflect a positive β-anisotropy parameter and a larger average kinetic energy release onto Cl*($^2P_{1/2}$) than onto Cl($^2P_{3/2}$).

tion, the correspondingly larger TOF causes isotopic overlap and ion fly-out. Both effects require a modification of the standard data analysis procedure. Details of the employed least-squares fit method employed in the correct analysis of the high-resolution data can be found in refs 33 and 38.

III. Results

Time-of-flight (TOF) profiles, $P_t(t)$, were monitored for both Cl($^2P_{3/2}$) ground state and Cl*($^2P_{1/2}$) excited spin−orbit state fragments for parallel ($\gamma = 0°$) and for perpendicular ($\gamma = 90°$) excitation geometries. Complete sets of four TOF profiles were obtained for each of the two dissociation wavelengths of 235 and 207 nm.

Figure 3 shows a set of TOF profiles for the dissociation wavelength of 235 nm at an acceleration voltage of 3 kV. The upper two traces in each panel represent the experimental raw data for parallel and perpendicular geometries for both ^{35}Cl and ^{37}Cl isotopes. For both spin−orbit states, the wings of the profiles of each isotope are more pronounced for the parallel excitation geometry than for the perpendicular excitation geometry. For any given fragment speed, v, the wing of a TOF profile, which is characterized by large Δt values, is contributed to by those fragments with large v_z components initially flying along the spectrometer axis, z, whereas the center of a TOF profile, which is characterized by small Δt values, is contributed to by those fragments with small v_z components initially moving perpendicular to the spectrometer axis, z. Hence, from Figure 3, it is evident that, for dissociation at 235 nm, fragments in both spin−orbit states are preferentially ejected along the electric field vector $\vec{E}$ of the dissociation laser: Profile wings are enhanced for parallel detection geometries; centers are enhanced for perpendicular detection geometries.

This situation is commonly described by a positive value of the anisotropy parameter, β, where the spatial fragment

$P_\theta(v,\theta,\varphi)$ distribution is expressed by its dependence on the angle θ:

$$P_\theta(v,\theta,\varphi) = \frac{P_v(v)}{4\pi v^2}[1 + \beta(v)P_2(\cos\theta)] \qquad (5a)$$

[Equation 5a ensures that both P_θ and P_v are normalized: $\iiint v^2 \sin\theta \, dv \, d\theta \, d\phi \, P_\theta(v,\theta) = \int dv \, P_v(v) = 1$.] Here, θ is the angle of the initial velocity vector of the fragment with the electric field vector, $\vec{E}$, of the dissociation laser, $P_v(v)$ is the speed distribution of the fragments, and P_2 is the second Legendre polynomial $P_2(x) = \frac{1}{2}(3x^2-1)$. If the coordinate system is rotated by the angle, γ, so that it is fixed to the spectrometer axis, z, rather than to the electric field vector, then the spatial distribution can be written in terms of the velocity component v_z:

$$P_\gamma(v,v_z) = \frac{P_v(v)}{2v}\left[1 + \beta(v)P_2\left(\frac{v_z}{v}\right)P_2(\cos\gamma)\right] \qquad (5b)$$

The distribution, $P_z(v_z)$, of the z component of the velocity, which is directly proportional to the TOF profile, $P_t(\Delta t)$, is obtained from P_γ by integrating eq 5b over the speed v:[33]

$$P_t(\Delta t) \propto P_z(v_z) = \int_{v_z}^{\infty} dv\left\{\frac{P_v(v)}{2v}\left[1 + \beta(v)P_2\left(\frac{v_z}{v}\right)P_2(\cos\gamma)\right]\right\} \qquad (5c)$$

From eqs 5b and 5c, it is obvious that both the spatial fragment distribution, P_γ, and the experimental TOF profile, P_t, become independent of the anisotropy parameter, β, if $P_2(\cos\gamma) = 0$, i.e., if γ is the magic angle of 54.7°. The same result is obtained for the sum $P_z^m(v_z) = \frac{1}{3}[P_z(v_z,\gamma = 0°) + 2P_z(v_z,\gamma = 90°)]$. The lowest trace in each panel in Figure 3 shows the magic angle TOF profile for Cl and Cl* fragments, accordingly composed from the experimentally observed profiles. Any influence of the spatial fragment distribution on the profile shape has been eliminated; thus the shape is only determined by the speed distribution of the fragments according to:

$$\frac{P_v(v)}{v} = -2\frac{dP_z^m(v_z)}{dv_z} \propto -2\frac{dP_t^m(\Delta t)}{d\Delta t} \qquad (6)$$

Basically, the speed distribution is given by the derivative of the magic angle TOF profile. Equation 6 only holds for an ideal experiment with unbiased detection of all fragments and if the apparatus response function is negligibly small compared to the width of the TOF profiles. More often than not, the simultaneous fulfillment of these conditions is not possible, and the data analysis becomes significantly more complex than the simplicity of eq 6 might suggest.[33] Nevertheless, for the conditions under which the profiles presented in Figure 3 were obtained, one can draw some qualitative conclusions based on the relationship established by eq 6. It is evident that the speed distributions for Cl ground state and for Cl* excited spin−orbit state fragments differ significantly from each other. While the ground-state Cl profiles are rather smooth and narrow, the excited-state Cl* profiles are broader and exhibit some modulation in the wings. Therefore, the corresponding Cl* speed distribution must be bimodal and contain contributions from fragments which are significantly faster than their Cl ground-state counterparts.

Figure 4 shows a set of TOF profiles for the dissociation wavelength of 207 nm at an acceleration voltage of 3 kV,
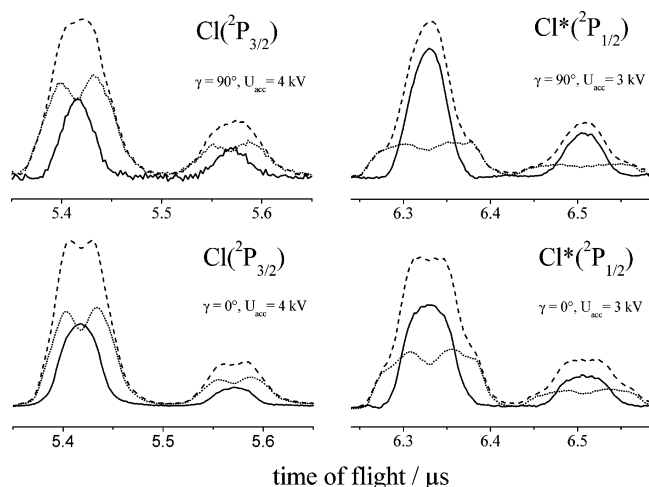
Figure 4. Experimental chlorine atom TOF profiles for Cl_2O dissociation at 6.0 eV (207 nm) for both spin−orbit states and detection geometries. Dashed lines are raw profiles and contain contributions from the 207 nm dissociation, as well as from the dissociation by the analysis laser at 235 nm. Dotted profiles are corresponding one-color profiles obtained for 235 nm dissociation alone. Solid profiles are obtained by subtracting the one-color signal from the two-color signal.

Figure 5. Experimental oxygen atom TOF profiles for Cl_2O dissociation wavelengths of 207 nm (filled circles) and 225.57 nm (open circles) for the $O(^3P_2)$ spin−orbit state at an acceleration voltage of 3 kV. The 207 nm data also contain some contribution from dissociation at the 225.57 nm detection wavelength. Profiles at both wavelengths are narrow and structureless and do not depend on the detection geometry, within experimental error. Signal intensities of the other spin−orbit states were too low to be analyzed.

Figure 6. Chlorine atom kinetic energy distributions following Cl_2O dissociation at 5.3 eV (235 nm). Distributions are shown for both $Cl(^2P_{3/2})$ and $Cl*(^2P_{1/2})$ spin−orbit states. Threshold energies corresponding to the dissociation limits (1a) and (3) are marked by dashed lines. For both electronic states, a bimodal behavior is observed such that the distributions can be composed of a slow and a fast component corresponding to channels (1a) and (3), respectively.

equivalent to the ones presented in Figure 3 for the dissociation wavelength of 235 nm. In Figure 4, the experimental profile contains contributions from both the 207 nm dissociation laser and the 235 nm probe laser. Therefore, the experiment was performed with (dashed line) and without the 207 nm dissociation laser present (dotted line), and in order to exclusively extract the profiles for 207 nm dissociation, the signals were subtracted from each other. Raw data and the corresponding difference profiles are both shown in Figure 4. Surprisingly, the difference profiles reflecting the dissociation dynamics at 207 nm (solid line) are narrower than the profiles for 235 nm dissociation. This means that the fragments generated by larger excitation energy are released with smaller translational energy than the fragments from 235 nm dissociation, although there is more energy deposited in the parent molecule. This is evidence of a new dissociation channel which is accessed at shorter dissociation wavelengths.

Only a weak dependence of profile shapes and widths on the Cl fragment electronic state or the detection geometry is observed. The 207 nm dissociation is, therefore, less specific with respect to product anisotropy and quantum state.

In addition to the Cl and Cl* profiles, oxygen atoms were also monitored. Figure 5 shows TOF profiles for dissociation wavelengths of 225 and 207 nm. Profiles are narrow and structureless. No influence of the detection geometry on the profile shapes could be detected. Signal levels were sufficiently large to be analyzed only for ground-state $O(^3P_2)$ atoms. For 207 nm dissociation, a very weak, broad shoulder was observed, which was not present for 225 nm dissociation. Otherwise, the 225 and 207 nm profiles are almost identical.

IV. Discussion

A. 5.3 eV Energetics. In Figure 6, state-specific kinetic energy distributions (KEDs) of $Cl(^2P_{3/2})$ and $Cl*(^2P_{1/2})$ fragments in both spin−orbit states are shown as obtained in the analysis procedure. Threshold energies corresponding to the dissociation limits (1a) and (3) are marked by dashed lines. Channel (1b) is not accessible for a dissociation wavelength of 235 nm. For both chlorine electronic states, a bimodal behavior is observed such that the KEDs can be composed of a slow and a *fast*
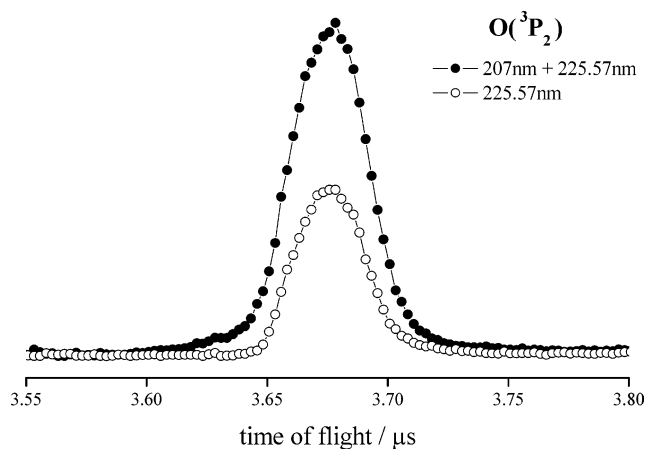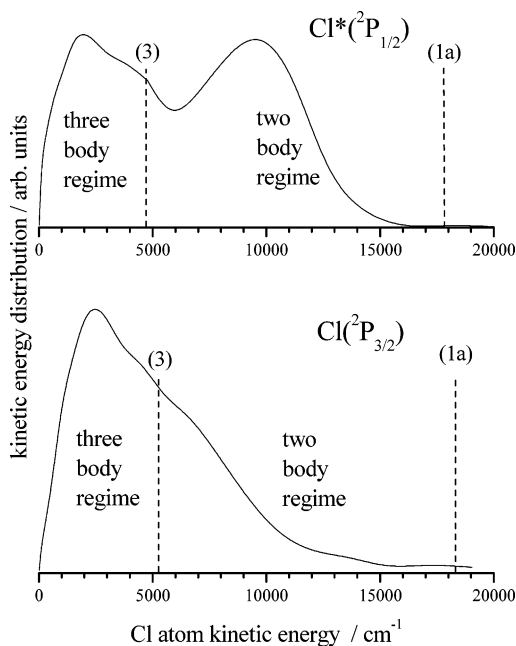
component which correspond to channels (1a) and (3), respectively. For $Cl(^2P_{3/2})$ ground-state atoms, the slow component dominates the overall distribution, whereas the opposite is the case for excited $Cl*(^2P_{1/2})$ excited spin−orbit state fragments.

This bimodal behavior has previously been observed by Tanaka et al. employing photofragment imaging.[14] For $Cl(^2P_{3/2})$ ground-state atoms, the agreement with the previous data is excellent, whereas for $Cl*(^2P_{1/2})$ excited spin−orbit state atoms, the agreement is only qualitative. Tanaka et al. observed significantly more fast Cl* than we did, and their average kinetic energy of the fast component is significantly larger than ours. However, their maximum total kinetic energy in the imaging
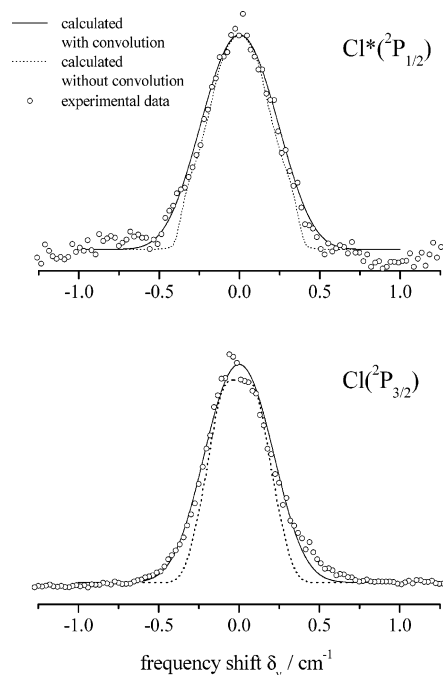
Photodissociation Dynamics of Cl₂O

J. Phys. Chem. A, Vol. 108, No. 39, 2004 **7959**

Figure 7. 5.3 eV (235 nm) dissociation: Comparison of experimental Doppler profiles with Doppler profiles calculated from the kinetic energy distributions of Figure 6. The excellent agreement confirms the correctness of the employed analysis procedure.

experiment exceeds the available energy for channel (1a).[14] To evaluate our data, we re-converted our KEDs, which have been derived from TOF measurements, into Doppler profiles as shown in Figure 7. This procedure yields Doppler profiles which agree very well with our experimentally observed Doppler profiles for both spin−orbit states if the effective laser line width for two-photon absorption (0.3 cm⁻¹ fwhm) is taken into account by appropriate convolution. This agreement is not trivial since the KED derived from the TOF data contains information not only about the excitation into the respective resonant intermediate states of the Cl fragment but also about the ionization step, hence, about the complete history of the fragment from fragmentation in the laser focus until impinging on the particle detector. The Doppler profiles, however, contain information about the neutral fragments only until they pass through the resonant intermediate electronic state. Perfect agreement between these two different sets of information necessarily means that no artifacts have been induced on the fragments following ionization out of the intermediate resonant state. Thus, any influence from Coulomb interaction between ionized fragments resulting from a too large charge density inside the laser focus can be ruled out in our experiment.

B. 5.3 eV Anisotropy. After the KEDs and the speed distributions, $P_v(v)$, have been determined, the anisotropy parameters, β, can be extracted from a single TOF profile from Figure 3 for any one detection geometry. The mean anisotropy parameters, $\langle \beta \rangle = \int dv \{P_v(v)\beta(v)\}$, exhibit the same value for both spin−orbit states and were found to be $\langle \beta_{Cl} \rangle = \langle \beta_{Cl*} \rangle = 0.7 \pm 0.2$. Unfortunately, the resolution of our measurements did not permit us to resolve the speed dependence, $\beta(v)$, of the anisotropy parameters. If a speed dependence exists, the variations of β with v should be smaller than ± 0.2, which is less than the variation from 0.7 to 1.5 observed by Okumura and co-workers in the 248 nm dissociation.[30] Again, there is qualitative agreement of our data with the values of Tanaka et al., who observed mean anisotropy parameters of 1.2 ± 0.2 for both spin−orbit states.[14] In fact, their value might be more

reliable than ours in view of the focusing conditions in our experiment. The focus diameter d_f in our experiment is estimated from the divergence $D \approx 10^{-3}$ of the laser beam and the focal length $f = 90$ mm of the focusing lens to be $d_f D \approx 100$ μm. The pulse energy of 200 μJ at 235 nm corresponds to ca. 2.5×10^{14} photons per laser pulse, resulting in a photon flux, Φ, of 3×10^{18} photons/cm². Taking into account the absorption cross section at 235 nm of $\sigma_{235} \approx 6 \times 10^{-19}$ cm², saturation of the dissociation step cannot be ruled out, the effect of which would be to reduce the value of the experimentally determined anisotropy parameter. Unfortunately, the focusing conditions of Tanaka et al. were not published.

Regardless of the quantitative disagreement between our values of the anisotropy parameters and the ones observed by Tanaka et al., that β is undoubtedly positive is sufficient to determine the nature of the Cl₂O excited state mainly involved in the dissociation at 235 nm. The value of the β parameter for an immediate decay on a single excited potential energy surface depends only on the geometry of the molecule and the direction of the transition dipole moment, which itself is determined by the symmetries of the initial and the final states in the excitation step. The β parameter is related to the angle, α, of the transition dipole moment, μ, with the fragment velocity vector **v** by[39]

$$\beta = 2P_2(\cos \alpha) \tag{7}$$

Therefore, if only one excited state is involved in the dissociation, the β parameter of 1.2 corresponds to $\alpha = 31°$ and the β parameter of 0.7 corresponds to $\alpha = 41°$. The sensitivity of the β parameter to the decay angle is large for the relevant decay angles, and, thus, a large deviation in β translates to a small deviation in α only. Therefore, experiment suggests that in the 235 nm dissociation of Cl₂O the decay angle, α_{235}, lies within the range of 30−40°. For a simultaneous excitation of more than one excited state, one needs to consider that the averaged β parameter reflects the correspondingly averaged decay angles for different symmetries.

For a nonimmediate decay involving passage through a conical intersection, the anisotropy parameter is a function of the rotational levels of the ClO counter fragment and can be calculated theoretically.[40] It must be negative for low J values and become positive for a large internal excitation of ClO. We could not experimentally observe any such J dependence due to the small rotational constant of the ClO counter fragment. Moreover, the fastest Cl fragments, which correspond to a small internal excitation of the ClO counter fragment, should exhibit a negative anisotropy parameter, which is in qualitative disagreement with our own observations as well as with the results obtained by Tanaka et al.[14]

C. 6.0 eV Energetics. The KEDs for 6.0 eV dissociation, after correction for 5.3 eV contribution, are shown in Figure 8. Again, the borderlines between the two-body radical decay (1a) and the three-body decay (3) are marked by dashed lines. The narrow TOF profiles translate into almost exclusive fragmentation via the three-body channel (3), accompanied by a small production of Cl in conjunction with highly excited ClO* radicals. Consequently, the bimodality present for both Cl and Cl* spin−orbit states is not ascribed to a competition between decay channels (1a) and (3), but rather to the three-body fragmentation mechanism (3) itself.

The oxygen atom TOF profiles shown in Figure 5 have not been converted to KEDs due to the small signal intensity, which did not allow an increase in the energy resolution by lowering the acceleration field strength. However, evaluating the maximum kinetic energy is possible from the main peak full width
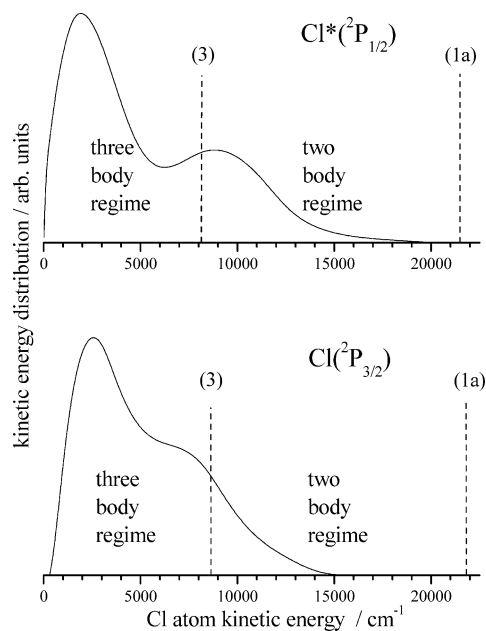
Figure 8. Chlorine atom kinetic energy distributions following Cl_2O dissociation at 6.0 eV (207 nm). Distributions are shown for both $Cl(^2P_{3/2})$ and $Cl*(^2P_{1/2})$ spin−orbit states. Threshold energies corresponding to the dissociation limits (1a) and (3) are marked by dashed lines.

at base of 70 ± 10 ns. This width corresponds to a maximum oxygen atom speed of 4000 ± 600 m/s and to a maximum oxygen atom kinetic energy of 10000 ± 3000 cm^{-1}, respectively. Based on the conservation of linear momentum, a hypothetical Cl_2 partner fragment would have to carry a maximum kinetic energy of 2300 ± 700 cm^{-1}, leaving a minimum internal energy of 22300 ± 3700 cm^{-1} in the Cl_2 fragment. Since this value supersedes the Cl_2 dissociation energy of 20000 cm^{-1}, a significant contribution of channel (2a) with production of ground-state $Cl_2(^1\Sigma_g^+)$ can be ruled out. However, the very small shoulders extending to 3.60 and 3.75 μs are proof of a minor contribution of channel (2a).

A two-body fragmentation is completely characterized by the knowledge of the energies of the reactants, the products, and the dissociating photon. Here, energy means not only enthalpy of formation, but also internal and kinetic energy, which can simultaneously be determined by the REMPI-TOF method employed in our experiment. However, for a three-body decay, the knowledge of these energetic quantities is not sufficient to characterize the fragmentation process. Moreover, concerted and sequential decay mechanisms will generally induce different kinetic energies onto the fragments.[15,16] Here, the terms "concerted" and "sequential" are used to distinguish between decay processes occurring within a rotational period of the parent molecule and decay processes which are delayed by more than one mean rotational period of the parent. Concerted decays may be subdivided into synchronous decays where both bonds strictly break in unison, such that the two terminating fragments behave identically, and asynchronous decays where this is not the case. Each decay mechanism can be characterized by a set of physically meaningful parameters, such as the bond angle when the molecule decays, the internal energy stored in the short-lived ClO intermediate, and the angle of rotation of the ClO intermediate before it breaks apart. The required analysis procedure has been described elsewhere in detail.[15,16] As a consequence, the observed kinetic energies can be analyzed in order to recognize the contribution of one or more of the

discussed mechanisms and the geometric parameters associated with the respective mechanisms.

For a synchronously concerted three-body decay, in addition to the energies mentioned above, one more quantity is needed for a complete characterization of the fragmentation process. In this case, the natural choice for this quantity is the bond (or decay) angle of the dissociating molecule. Any one decay angle correlates to a precise fragment kinetic energy. Therefore, from an experimentally observed kinetic energy distribution, one can extract a corresponding decay angle distribution if the decay mechanism is known to be synchronous. Cl fragment kinetic energies $E_{kin}(Cl)$ acquired in a synchronous three-body decay of Cl_2O are restricted to a certain energy range, which is determined by the fragment masses, m_{Cl} and m_O, and by the total kinetic energy, ϵ, of all fragments. The total kinetic energy is the available energy E_{av} diminished by internal fragmentation excitation.[15] Here, $E_{av} = h\nu - \Delta H$ is defined as the difference of the photon energy $h\nu$ and the dissociation enthalpy given in eq 3. Generally, the Cl fragment kinetic energy $E_{kin}(Cl)$ is restricted to the range $^1/_2\epsilon/(1 + 2m_{Cl}/m_O) \leq E_{kin}(Cl) \leq ^1/_2\epsilon$, which for dissociation into $Cl(^2P_{3/2}) + Cl*(^2P_{1/2}) + O(^3P_2)$ at 6.0 eV translates to 1300 cm$^{-1} \leq E_{kin}(Cl) \leq 6850$ cm^{-1} Clearly, the quality of fitting a Gaussian distribution of decay angles to the observed Cl KEDs is poor, as shown in the upper panel of Figure 9. Whereas there is no a priori reason to restrict the decay angle distribution to a Gaussian distribution, the significant contribution of slow Cl fragments ($E_{kin}(Cl) < 1300$ cm^{-1}) cannot be explained by a synchronous three-body decay for any decay angle distribution.

For a sequential three-body decay, in addition to the energetic quantities, two more quantities are required for completely characterizing the fragmentation process. Two physically meaningful quantities are the internal energy deposition, E_{ClO}, in the short-lived ClO intermediate and the angle of rotation, φ, of the ClO intermediate before it breaks apart. Any one set of these quantities again correlates to a precise Cl fragment kinetic energy. A characteristic feature of a sequential (planar) three-body decay is a symmetric kinetic energy distribution for the Cl fragment generated in the second step, which reflects forward−backward symmetry of the decay of the freely rotating ClO intermediate. For a sequential decay, the restriction for the Cl kinetic energy is $0 \leq E_{kin}(Cl) \leq \epsilon m_{ClO}/M$ where M is the mass of the Cl_2O parent molecule.[15] For dissociation into $Cl(^2P_{3/2}) + Cl*(^2P_{1/2}) + O(^3P_2)$ at 6.0 eV, this energy range is $E_{kin}(Cl) \leq 8150$ cm^{-1}. The resulting fit is shown in the middle panel of Figure 9. Although its quality is higher than for the synchronously concerted case, the symmetry properties of the second step KED allow either the low-kinetic energy side or the high-kinetic energy side to be described well, but not both for the same decay parameter distribution. Since the description of the experimental KED by a sequential decay yields a more reasonable result than for the synchronous decay, an asynchronously concerted decay corresponding to a moderate restriction of the free rotation of the ClO intermediate to the most probable angle of rotation prior to the decay of the ClO intermediate should result in a good description of the experimental KED. Modeling such an asynchronous concerted decay with Gaussian distributions of, φ, and E_{ClO} peaking at 105° and 0.75ϵ, respectively, the fit shown in the lower panel of Figure 9 is obtained, which is the best description to the experimental data. The widths (fwhm) of the Gaussian distributions are 30° and 0.14ϵ, respectively.

The energy deposition, E_{ClO}, refers to the energy of the separated atoms Cl + O in their respective quantum states. If
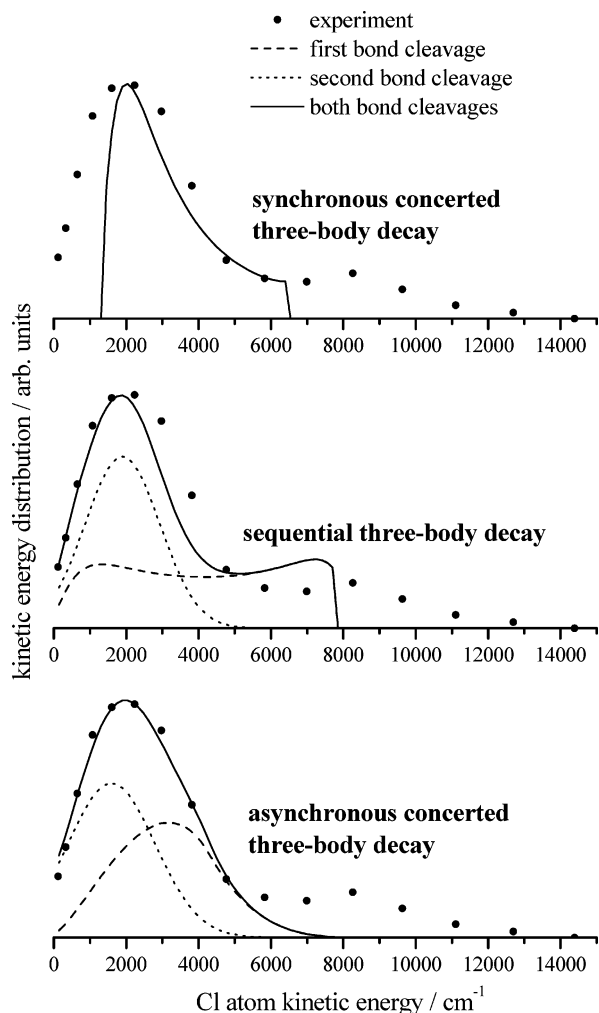
Figure 9. Fits of different decay models to the experimental Cl fragment kinetic energy distribution for Cl$_2$O + $h\nu$(207 nm) → Cl(^{2}P$_{3/2}$) + Cl*(^{2}P$_{1/2}$) + O(^{3}P$_2$). A good description of the experimentally determined KED is only achieved assuming an asynchronous, concerted three-body decay mechanism.

the dissociation energy, D_0(ClO) = 22180 cm^{-1}, is added to E_{ClO}, one obtains a ClO excitation with respect to its ground state of ca. 33000 cm^{-1}, which is only little more than the ClO-(A$^2\Pi$) excited state at 31480 cm^{-1}.[17] The remaining energy of the order of 1500 cm^{-1} would be sufficient to populate three vibrational or ca. 50 rotational levels. The lifetimes of the first six vibrational levels of ClO(A$^2\Pi$) have been determined to vary between 0.2 and 2 ps, whereas a rotational period for ClO-(A$^2\Pi$) with one quantum of nuclear rotation lasts ca. 25 ps. These numbers suggest that the asynchronous concerted three-body decay might produce ClO(A$^2\Pi$) + Cl(^{2}P) in the first step, followed by ClO(A$^2\Pi$) predissociation on the picosecond time scale.

D. 6.0 eV Anisotropy. The mean anisotropy parameters for Cl and Cl* production at 207 nm were found to be 0.2 ± 0.2. Again, no variation of the β parameter with fragment speed could be observed. It must be taken into account, however, that now each decay produces two individual fragments which are likely to be differently distributed in space. Thus, the β parameter determined in our experiment is an average of these two physically different species produced by the three-body decay. Of course, the physical properties of the final fragments are not independent of each other, and the first fragmentation event must necessarily induce identical spatial distribution with respect to the electric field vector of the dissociation laser onto
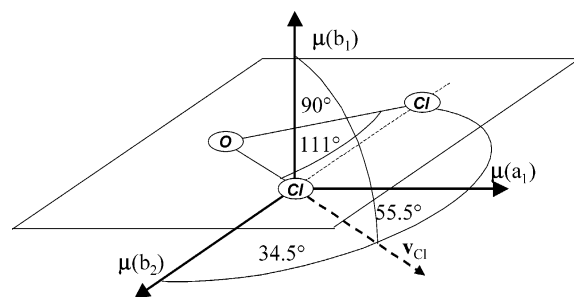
the primary fragments. The effect of the delayed fragmentation of the intermediate ClO particle can be evaluated using the relation[41−43]

$$\beta_\tau = \beta\left(\frac{1 + \omega^2\tau^2}{1 + 4\omega^2\tau^2}\right) \qquad (8)$$

where ω is the frequency of rotation of the intermediate, and τ is its lifetime. β_τ is the accordingly reduced anisotropy parameter, and β is the anisotropy parameter for immediate decay, as defined in eq 7. From the previous paragraph, we know that $\omega\tau \approx 0.3$. Thus, the effect of delayed fragmentation of the intermediate is estimated to be a reduction of the immediate β parameter by 20%: $\beta_\tau = 0.8\beta$. If we assume for simplicity that the first fragmentation event takes place immediately with the excitation, then the experimentally observed anisotropy parameter, $^1\!/_2(\beta_\tau + \beta)$, will be 10% lower than the anisotropy parameter, β, characterizing the excitation step. Since the experimentally determined averaged anisotropy parameter was determined to be 0.2 ± 0.2, this small effect might be neglected in view of the much larger experimental uncertainty, and we conclude that the anisotropy parameter, β, characterizing the excitation step of Cl$_2$O at 207 nm is 0.2 ± 0.2.

Focusing conditions that might be responsible for reducing the anisotropy parameter observed for the 235 nm dissociation are not likely to play an important role at 207 nm. First, the pulse energy at 207 nm is lower than that at 235 nm, and second, the Cl$_2$O absorption cross section at 207 nm is smaller than that at 235 nm. Even if the observed small deviation at 235 nm were entirely due to saturation of the dissociation step, a possible, but necessarily even smaller, effect at 207 nm can safely be ignored.

E. Electronic Structure. The transition dipole moment, μ, of a dipole-allowed electronic transition must have appropriate symmetry properties, depending on the symmetries of the initial and the final states. For transitions originating from the totally symmetric Cl$_2$O(X^{1}A$_1$) ground state, the symmetry property of the transition dipole moment must be the same as that of the target state, i.e., a$_1$ for a transition to an A$_1$ state, b$_1$ for a transition to a B$_1$ state, and b$_2$ for a transition to a B$_2$ state. The corresponding orientation of the transition dipole moments in the molecular frame is shown in Figure 10. Consequences for spatial distributions of photodissociation fragments and for β anisotropy parameters, respectively, are discussed below.

The Cl$_2$O bond length and bond angle were determined to be 169.587 pm and 110.886°, respectively.[44] The transition dipole moment for a A$_1$ ← A$_1$ transition (a$_1$ symmetry) lies parallel to the C$_2$ symmetry axis. The angle, α(a$_1$), of μ(a$_1$) with the recoil velocity, **v**, of a Cl fragment, taken to be parallel to the Cl−O bond, is equal to half of the Cl−O−Cl bond angle, and thus amounts to α(a$_1$) = 55°, close to the magic angle, resulting in an anisotropy parameter of β*(a$_1$) = 0.0, according

Figure 10. Geometry, symmetry properties, and orientation of transition dipole moments for the Cl$_2$O(X^{1}A$_1$) electronic ground state.

TABLE 1: Compilation of Theoretical Results for the Excitation of Cl$_2$O: Spectroscopic Terms, Limiting Anisotropy Parameters, β^*, for Immediate Decay from Ground-State Geometry, Vertical Excitation Energies, ΔE, and Oscillator Strengths, f^a

	β^*		Tomasello et al.[5]		Toniolo et al.[10]		Del Bene et al.[12]		Nickolaisen et al.[11]	
			ΔE/eV	f	ΔE/eV	f	ΔE/eV	f	ΔE/eV	f
1	-1	1^1B_1	2.92	0.00010	2.68	0.00110	2.82	0.00008	3.42	0.00014
2	$+1$	1^1B_2	4.42	0.01060	4.39	0.11000	4.23	0.01017	4.98	0.00770
3		1^1A_2	4.57		4.39		4.23		4.97	
4	0	2^1A_1	4.81	0.00050	4.47	0.00059	4.66	0.00177	5.45	0.00009
5		2^1A_2	5.69		4.88		5.01		5.88	
6	-1	2^1B_1	6.97	0.00450	6.41	0.00063			7.35	0.00526
7	0	3^1A_1	7.14	0.00040	5.35	0.00001				
8	$+1$	2^1B_2	7.55	0.20660	6.77	0.00900			7.98	0.00001
9	-1	3^1B_1	7.85	0.04530	6.58	0.13000				
10	-1	4^1B_1	8.25	0.00000	7.70	0.00240				
11		3^1A_2	8.62		6.44					
12	0	4^1A_1	8.73	0.01030	6.42	0.00170				
13	$+1$	3^1B_2	9.20	0.03440	7.04	0.07200				

^{a} The $\beta^*(\Delta E)$ dependence is illustrated in figure 2 by square symbols.

to eq 7. The asterisk indicates that the respective value is calculated for an immediate decay from the ground-state geometry and does not account for any dynamical effects or for effects due to the initial conditions of the parent, which will be discussed below. Applying the same reasoning to a $B_1 \leftarrow A_1$ transition, the transition dipole moment of b_1 symmetry is oriented perpendicular to the molecular plane. Then, the angle, $\alpha(b_1)$, of $\mu(b_1)$ with **v** is 90°, and $\beta^*(b_1) = -1.0$. For a $B_2 \leftarrow A_1$ transition, the transition dipole moment of b_2 symmetry is oriented parallel to the line connecting the two Cl atoms. The angle, $\alpha(b_2)$, of $\mu(b_2)$ with **v** is 34.5°, and $\beta^*(b_2) = +1.0$. The determination of anisotropy parameters is therefore a useful tool for investigating the nature of electronically excited states in photodissociation experiments. The dipole-forbidden $A_2 \leftarrow A_1$ transition will become allowed upon a reduction of molecular symmetry as it occurs for excitation of the anti-symmetric Cl−O−Cl stretch vibrational mode. However, even at room temperature, only 3% of the Cl$_2$O molecules will be excited in the anti-symmetric stretch due to the relatively large vibrational quantum of 85 meV;[45] for the jet-cooled molecules in our experiment, only zero-point motion will occur. Hence, we conclude that the $A_2 \leftarrow A_1$ transition does not significantly contribute to the optical excitation.

The observed β parameter values are a result of the simultaneous excitation of different electronically excited states of the parent molecule. In principle, aside from simultaneous excitation of more than one electronically excited state, there are other effects which might also influence the β parameter, in addition to the relationships outlined above. However, none of these effects can explain the experimental observations. First, dynamic effects will be considered. If the excited potential energy surface exhibits a gradient with respect to the bond angle, the parent molecule might change its geometry prior to fragmentation if its lifetime is at least of the order of a vibrational period. Note, that for an immediate decay, the additional motion alone that will be inferred onto the nuclei by the gradient on the upper potential energy surface is not sufficient to noticeably change the β parameter, except for near-threshold conditions where the repulsive force is very small. This latter effect can safely be ignored for our experimental conditions. Dynamic effects might decrease or increase the value of the limiting β^* anisotropy parameter depending on whether it increases or decreases the angle, α. Some qualitative arguments on this issue can be obtained following Walsh's rules,[46] which predict a bent geometry for molecules with 20 valence electrons and a linear geometry for 21 valence electrons, which

agrees with the bent ground-state geometry of the 20 valence electron Cl$_2$O molecule. Accordingly, the electronically excited molecule should prefer a linear, or at least a more linear, configuration with an increased bond angle. The effect on the β parameters of the corresponding transitions would be an increase of $\beta(b_2)$ for the $B_2 \leftarrow A_1$ transition and a decrease of $\beta(a_1)$ for the $A_1 \leftarrow A_1$ transition, while the perpendicular $B_1 \leftarrow A_1$ transition would remain unaffected by the nuclear rearrangement. While this behavior has in fact been predicted from trajectory calculations based on the potential energy surfaces of Toniolo et al.,[6] it contradicts our own, as well as previously obtained, experimental evidence.[13,14,30] A second effect is the decrease of the β parameter by initial parent molecule motion due to translational, rotational, or vibrational excitation. This effect can be ignored in our case for two reasons. First, the parent molecule is cooled in the supersonic expansion to temperatures below 15 K, and second, the dissociation threshold is much smaller than the photon energy, so that even under bulk conditions the fragment momentum induced by repulsion in the dissociation coordinate would be much larger than the one induced by parent molecule motion. A third effect influencing the value of β that needs to be considered is connected to the nonzero lifetime of the parent molecule for nonimmediate decay. Previous experimental and theoretical work performed for smaller excitation energies suggests, however, that Cl$_2$O photodissociation is direct and prompt.[6,9] Therefore, we assume it to be very unlikely that, for the larger excitation energies used in our study, lifetime effects should be of any relevance for the experimentally observed β parameter.

Our interpretation of simultaneous excitation is supported by the large density of states above an excitation energy of 4 eV which are predicted for all theoretical calculations, as compiled in Table 1. The respective limiting β^* anisotropy parameters, which would be expected for immediate decay from ground-state geometry following a pure excitation into a single excited state, are shown together with experimentally determined anisotropy parameters in Figure 2. The β parameters at 235 and 207 nm, which have been determined in this work, are marked by filled circles. Experimentally, the anisotropy parameter increases from -1 at the lowest excitation energies around and below 3 eV to positive values between 3.5 and 6.5 eV, with a maximum of about $+1$ at 5 eV. This $\beta(E)$ dependence is firmly established by experiments; no less than six research groups have contributed to this result without any qualitative contradiction among them. At first sight, this result may easily be rationalized by a series of the three dipole-allowed one-electron

Photodissociation Dynamics of Cl$_2$O

J. Phys. Chem. A, Vol. 108, No. 39, 2004 **7963**

excitations out of the four highest occupied molecular orbitals $(2a_2)^2$ $(9a_1)^2$ $(7b_2)^2$ $(3b_1)^2$ into the lowest unoccupied $(10a_1)$ molecular orbital. This series would consist of a sequence of transitions to the 1B$_1$, 1B$_2$, and 2A$_1$ states (numbers 1, 2, and 4 in Table 1) with corresponding β^* parameters -1, $+1$, and 0. However, the excitation dynamics must be more complex than that. The energetic separation of the four highest occupied molecular orbital is well-known from photoelectron spectroscopy and covers an energy range of only 2.8 eV. This contradiction becomes apparent when individual theoretical results are compared to experimental data. Whereas the predictions of Nickolaisen et al. agree well with the observed fragmentation dynamics for excitation energies around 5 eV, their assignment of the first small absorption feature around 3 eV as resulting from triplet $\leftarrow$ singlet excitation must be regarded as erroneous. On the other hand, the assignment of this feature to the $10a_1 \leftarrow 3b_1$ excitation agrees very well the experiments of Davis et al. and of Aures et al., but goes along with incorrect predictions of the fragmentation dynamics around 5 eV. For this energy range, predicted zero or negative β parameter values are in marked contrast with the experimentally observed positive values. Considering the second series of one-electron excitations into the second lowest unoccupied molecular orbital $(8b_2)$ results in a sequence of transitions to 3A$_1$, 2B$_2$, and 3B$_1$ states (numbers 7, 8, and 9 in Table 1) with corresponding β^* parameters 0, $+1$, and -1. In fact, this explanation extends the range where positive β parameters will be observed well into the energy range above 6 eV and matches the experimental observations well. In this case, energies and oscillator strengths for the 2B$_2$ and 3B$_1$ states as calculated by Tomasello et al. are in much better agreement with experimental observations than the data published by Toniolo et al. In any case, the influence of the 2B$_1$ state, which both authors calculate to lie between the two one-electron sequences into the 10a$_1$ and 8b$_2$ orbitals, respectively, has not been observed experimentally. Either this state, being the first involving higher excitations than the 8b$_2$ molecular orbital, mixes strongly with other high-lying excited states or the rather small oscillator strength, in combination with unfavorable Franck$-$Condon factors, might reduce the intensity of this perpendicular transition to such an extent that it is too small to be experimentally observable.

Hence, we conclude that at 235 nm Cl$_2$O excitation mainly occurs via the transitions $10a_1 \leftarrow 7b_2$ and $10a_1 \leftarrow 9a_1$. The observed β parameter of $+0.7$ suggests that the former makes the dominant contribution. Its large oscillator strength might easily compensate for the somewhat larger deviation of its calculated excitation energy from the photon energy. The situation can largely be rationalized by the assignment depicted in Figure 1. According to Tanaka et al., the ^{1}B$_2$ state correlates with a ClO(X$^2\Pi$) + Cl*(^{2}P$_{1/2}$), and ground-state Cl(^{2}P$_{3/2}$) will be produced by nonadiabatic long-range interactions, which play a role only in a restricted range of the initially excited potential energy surface.[14] Therefore, the difference in the KEDs for Cl*(^{2}P$_{1/2}$) and Cl(^{2}P$_{3/2}$) atoms reflects the limited interaction region of the corresponding PES. The excitation at 207 nm, in the next absorption band on the short-wavelength side, is likely to promote the 7b$_2$ electron into the second unoccupied 8b$_2$ orbital. Although suggested by theory, no evidence is found for electronic excitation into higher orbitals. Similarly to the situation at 235 nm, a strong, dominant 8b$_2 \leftarrow$ 9a$_1$ transition might also be responsible for masking the influence of higher excitations. In any case, theoretical results must further be improved in order to satisfactorily describe the dissociation dynamics of Cl$_2$O for excitation energies between 3 and 7 eV.

V. Conclusion

The photodissociation of Cl$_2$O has been investigated by resonance-enhanced multiphoton ionization in combination with time-of-flight measurements for the excitation energies 5.3 eV (235 nm) and 6.0 eV (207 nm) in adjacent regions of the first and the second absorption bands. At 5.3 eV, the main primary dissociation channel is ClO + Cl(^{2}P$_{1/2}$). A significant portion of Cl(^{2}P$_{1/2}$) undergoes conversion to ground-state Cl(^{2}P$_{3/2}$) during fragmentation. The decay is characterized by a positive anisotropy parameter of 0.7 ± 0.2. Excitation proceeds via the transitions $10a_1 \leftarrow 7b_2$ and $10a_1 \leftarrow 9a_1$. At 6.0 eV, the main dissociation channel is the three-body decay into 2Cl + O. The decay mechanism is of an asynchronous concerted type, possibly with ClO(A$^2\Pi$) as intermediate fragment. The decay is characterized by a small positive anisotropy parameter of 0.2 ± 0.2. Excitation proceeds mainly via the transition 8b$_2 \leftarrow$ 7b$_2$.

References and Notes

(1) Tomasello, P.; Ehara, M.; Nakatsuji, H. *J. Chem. Phys.* **2003**, *118*, 5811.

(2) Cooksey, C. C.; Reid, P. J. *J. Phys. Chem. A* **2003**, *107*, 5508.

(3) Chau, F.-T.; Dyke, J. M.; Lee, E. P. F.; Mok, D. K. W. *J. Chem. Phys.* **2003**, *118*, 4025.

(4) Aures, R.; Gericke, K.-H.; Maul, C.; Trott-Kriegeskorte, G.; Kawasaki, M.; Nakano, Y. *J. Chem. Phys.* **2002**, *117*, 2141.

(5) Tomasello, P.; Ehara, M.; Nakatsuji, H. *J. Chem. Phys.* **2002**, *116*, 2425.

(6) Collaveri, C.; Granucci, G.; Persico, M.; Toniolo, A. *J. Chem. Phys.* **2001**, *115*, 1251.

(7) Smith, G. D.; Tablas, F. M. G.; Molina, L. T.; Molina, M. J. *J. Phys. Chem. A* **2001**, *105*, 8658.

(8) Roth, M.; Einfeld, T.; Gericke, K.-H.; Maul, C. *Phys. Chem. Earth* **2001**, *C26*, 513.

(9) Aures, R.; Gericke, K.-H.; Kawasaki, M.; Maul, C.; Nakano, Y.; Trott-Kriegeskorte, G.; Wang, Z. *Phys. Chem. Commun.* **2001**, *22*, 1.

(10) Toniolo, A.; Persico, M.; Pitea, D. *J. Phys. Chem. A* **2000**, *104*, 7278.

(11) Nickolaisen, S. L.; Miller, C. E.; Sander, S. P.; Hand, M. R.; Williams, I. H.; Francisco, J. S. *J. Chem. Phys.* **1996**, *104*, 2857.

(12) Del Bene, J. E.; Watts, J. D.; Bartlett, R. *J. Chem. Phys. Lett.* **1995**, *246*, 541.

(13) Nelson, C. M.; Moore, T. A.; Okumura, M.; Minton, T. K. *J. Chem. Phys.* **1994**, *100*, 8055.

(14) Tanaka, Y.; Kawasaki, M.; Matsumi, Y.; Fujiwara, H.; Ishiwata, T.; Rogers, L. J.; Dixon, R. N.; Ashfold, M. N. R. *J. Chem. Phys.* **1998**, *109*, 1315.

(15) Maul, C.; Gericke, K.-H. *Int. Rev. Phys. Chem.* **1997**, *16*, 1.

(16) Maul, C.; Gericke, K.-H. *J. Phys. Chem. A* **2000**, *104*, 2531.

(17) Howie, W. H.; Lane, I. C.; Newman, S. M.; Johnson, D. A.; Orr-Ewing, A. J. *Phys. Chem. Chem. Phys.* **1999**, *1*, 3079.

(18) Renard, J. J.; Bolker, H. I. *Chem. Rev.* **1976**, *76*, 487.

(19) Wang, D.-C.; Lee, E. P. F.; Chau, F.-T., Mok, D. K. W.; Dyke, J. M. *J. Phys. Chem. A* **2000**, *104*, 4936.

(20) Motte-Tollet, F.; Delwiche, J.; Heinesch, J.; Hubin-Franskin, M.-J.; Gingell, J. M.; Jones, N. C.; Mason, N. J.; Marston, G. *Chem. Phys. Lett.* **1998**, *284*, 452.

(21) Cornford, A. B.; Frost, D. C.; Herring, F. G.; McDowell, C. A. *J. Chem. Phys.* **1971**, *55*, 2820.

(22) Goodeve, C. F.; J Wallace, I. *Trans. Faraday Soc.* **1930**, *26*, 254.

(23) Finkelnburg, W.; Schumacher, H. J.; Stieger, G. *Z. Phys. Chem., Abt. B 15*, 127.

(24) Lin, C.-L. *J. Chem. Eng. Data* **1976**, *21*, 411.

(25) Molina, L. T.; Molina, M. J. *J. Phys. Chem.* **1978**, *82*, 2410.

(26) Knauth, H.-D.; Alberti, H.; Clausen, H. *J. Phys. Chem.* **1979**, *83*, 1604.

(27) Nee, J. B. *J. Quant. Spectrosc. Radiat. Transfer* **1991**, *46*, 55.

(28) DeMore, W. B.; Sander, S. P.; Golden, D. M.; Hampson, R. F.; Kurylo, M. J.; Howard, C. J.; Ravishankara, A. R.; Kolb, C. E.; Molina, M. J. *Chemical Kinetics and Photochemical Data for Use in Stratospheric*

Modeling, Evaluation Number 12; JPL Publication 97-4; Jet Propulsion Laboratory: Pasadena, 1997.

(29) Davis, H. F.; Lee, Y. T. *J. Chem. Phys.* **1996**, *105*, 8142.

(30) Moore, T. A.; Okumura, M.; Minton, T. K. *J. Chem. Phys.* **1997**, *107*, 3337.

(31) Cady, G. H. *Inorg. Synth.* **1957**, *5*, 156.

(32) Haas, T.; Maul, C.; Gericke, K.-H.; Comes, F. J. *Chem. Phys. Lett.* **1993**, *202*, 108.

(33) Roth, M.; Maul, C.; Gericke, K.-H. *Phys. Chem. Chem. Phys.* **2002**, *4*, 2932.

(34) Maul, C.; Haas, T.; Gericke, K.-H. *J. Phys. Chem A* **1997**, *101*, 6619.

(35) Arepalli, S.; Presser, N.; Robie, D.; Gordon, R. *J. Chem. Phys. Lett.* **1985**, *118*, 88.

(36) Ascenzi, D.; Regan, P. M.; Orr-Ewing, A. *J. Chem. Phys. Lett.* **1999**, *310*, 477.

(37) Bamford, D. J.; Jusinski, L. E.; Bishel, W. K. *Phys. Rev. A: At., Mol., Opt. Phys.* **1986**, *34*, 185.

(38) Matsumi, Y.; Shamsuddin, S. M.; Sato, Y.; Kawasaki, M. *J. Chem. Phys.* **1994**, *101*, 9610.

(39) Bersohn, R.; Lin, S. H. *Adv. Chem. Phys.* **1969**, *16*, 67.

(40) Mordaunt, D. H.; Ashfold, M. N. R.; Dixon, R. N. *J. Chem. Phys.* **1996**, *104*, 6460.

(41) Jonah, C. *J. Chem. Phys.* **1971**, *55*, 1915.

(42) Busch, G. E.; Wilson, K. R. *J. Chem. Phys.* **1972**, *56*, 3626.

(43) Busch, G. E.; Wilson, K. R. *J. Chem. Phys.* **1972**, *56*, 3638.

(44) Nakata, M.; Sugie, M.; Takeo, H.; Matsumura, C.; Fukuyama, T.; Kuchitsu, K. *J. Mol. Spectrosc.* **1981**, *86*, 241.

(45) Xu, Y.; McKellar, A. R. W.; Burkholder, J. B.; Orlando, J. J. *J. Mol. Spectrosc.* **1996**, *175*, 68.

(46) Walsh, A. D. *J. Chem. Soc.* **1953**, 2288.